J. Min. Metall. Sect. B-Metall. 58 (3) (2022) 367 - 378

Journal of Mining and Metallurgy, Section B: Metallurgy

FUNCTIONALLY GRADED AZ91/WC NANOCOMPOSITE FABRICATED VIA FRICTION STIR PROCESSING USING A NOVEL WAY

A.D. Subhi*, M.H. Abdulkareem, H.A. Hussein

University of Technology-Iraq, Department of Production Engineering and Metallurgy, Baghdad, Iraq

(Received 22 March 2022; Accepted 28 July 2022)

Abstract

In this work, functionally graded AZ91/WC nanocomposites were prepared by a novel multi-step chamber diameter reduction method. The WC nanoparticles were packed into chambers with graded diameters and processed by friction stirring using a tool with four-sided grooved probe. The functionally graded nanocomposites were fabricated at different tool rotational speeds (830, 960 and 1160 rpm) at a constant traverse speed and plunge depth of 40 mm/min and 0.1 mm, respectively. The properties of the functionally graded samples and AZ91 Mg alloy were evaluated by optical and scanning electron microscopy, energy dispersive spectroscopy, and other tests such as hardness, pin on disc wear and potentiodynamic polarization tests. The results showed that α-Mg and graded distribution of WC nanoparticles improved as the tool rotational speed increased. The hardness increased slightly with increasing the rotational speed of the tool. The results also revealed that the wear rate was decreased and corrosion resistance was improved by adding WC nanoparticles. Abrasive wear mode was the main mode of material removal during dry sliding, while cracks and pits were the main features of the corroded surface.

Keywords: *Friction stir processing; Functionally graded composite; Nanocomposite; AZ91 Mg alloy; Tungsten carbide*

1. Introduction

The growth of our society and culture is inextricably linked with engineering materials. The growing need to reduce emissions and improve performance has promoted engineers to develop new, lightweight, high-performance materials with significant characteristics for industrial applications [1, 2]. In contrast, surface engineering processes have a vigorous influence on the life of components in several situations [3, 4]. However, the characteristics that materials should possess are enhanced strength, toughness, hardness, and thermal, corrosion and wear resistance etc. Materials with lower density have the advantage of yielding higher load capacity, whereas higher strength and stiffness materials result in proper performance and safety characteristics. These characteristics can be combined through the use of the concept of functionally graded materials (FGMs) [5, 6].

The FGM, an advanced class of composite materials developed by the Japanese in 1984, is a concept for combining incompatible characteristics in the same material. It is distinguished by a spatial gradient in composition and/or structure along at least one direction. The gradient of a property in a material result from the dependence of position on atomic order, chemical composition, or microstructure [7]. The FGM also minimizes the thermal stresses that arise and provides improved bonding among different phases, resulting in enhanced fracture resistance and toughness along a gradual variance direction. Therefore, material responses can be tailored based on the design criteria according to FGM help [8, 9].

There are various processing methods for FGM fabrication. These methods have seen improvements in design, development, and uses to overcome challenges encountered by traditional methods. Various fabrication processes are centrifugal casting [10], powder metallurgy (PM) [11], solid free foam (SFF) [12], physical and chemical vapor deposition (PVD/CVD) [13], 3D printing [14], electrophoretic deposition (EPD) [15], and friction stir processing (FSP) [16], etc.

The FSP can be used for FGM fabrication as the reinforcement particles are packed into specific locations along the stirring pathway. It has developed from the principles of friction stir welding (FSW) and has grown as a favorable tool for changing the surface microstructure of metals and alloys [17]. Generally, FSP is performed by plunging a cylindrical rotating tool without a pin or with a pin having geometrical features at its end to the required depth in the

Corresponding author: akeel.d.subhi@uotechnology.edu.iq

https://doi.org/10.2298/JMMB2203220018S

transverse direction by applying the appropriate load causing severe deformation of the stirring area. Moreover, FSP has the merits of adjusting mechanical characteristics of the materials surface using optimized tool design and controlled process parameters. It also enhances the materials mixing and disperse of the reinforcing phase within the material surface without excessive interaction [18].

To date, several metallic materials are widely considered as matrices for FGMs fabrication as each alloy has its own characteristics [19]. Magnesium and its alloys are distinguished by low density, high specific strength, good weldability, machinability and castability. The problem with Mg is related to its inherent brittleness [20]. The fabrication of composites within the surface of Mg-based alloys are a new class of materials in non-ferrous alloys that address surface problems associated with Mg brittleness. The FSP can be applied to yield surface composite inside the surface of Mg alloys resulting in improved surface characteristics of the processed area [21].

Several reinforcements are widely used in micro/nano sizes including oxides, borides, carbides, silicides, nitrides, and intermetallics to improve mechanical, chemical, thermal, and tribological properties of materials. Other reinforcements such as hydroxyapatite, bamboo leaf ash, carbon fibers and marble dust have also been increasingly used. The broad uses of reinforcements reflect their benefits in various engineering and scientific sectors such as automobiles, aircraft, marine, civil, and structure engineering [22-24]. There are limited attempts to manufacture FGM using FSP. J. Gandra et al. [16] investigated the functionally graded (FG) AA5083 Al alloy/SiC fabricated using FSP by making square shaped grooves on the surface of the AA5083 Al alloy. They concluded that the thickness of the FG layer relies on the SiC particle size and the tool geometry used. M. Salehi et al. [25] studied the SiC particles distribution and hardness profile of FG 6061 Al alloy/SiC nanocomposites fabricated utilizing multistep FSP by making grooves and using tools with different probe heights. They disclosed that the composition of FG sample was varied from 18 to 0 wt%SiC along five layers and the hardness value in sample was obtained constant along the thickness. V. Bikkina et al. [26] addressed that an increment in the FSP passes number leads to a uniform gradient of SiC particle distribution in the FG 6082 Al alloy/SiC composite fabricated using a novel multi-step FSP. The hardness values and wear properties were affected by the number of passes performed. A.M. Jamili et al. [27] reported that such gradient in the microstructure/texture evolution due to the influence of mechanical post-treatment on the FSPed Mg-4.37 wt%Y-2.9 wt%RE-0.3 wt%Zr alloy indicates that the FSP plus compression loading is a suitable method for fabrication of micro-scale FGMs.

The present work highlights a new method for fabricating functionally graded AZ91/WC nanocomposites. In this method, consecutive graded chambers were fabricated along the FSP pathway and packed with WC nanoparticles. The FSP was performed along the path of these chambers to fabricate a gradient of WC nanoparticles in the surface of the AZ91 Mg alloy. The fabricated functionally graded nanocomposites (FGNCs) were characterized by optical microscopy (OM), scanning electron microscopy (SEM), and energy dispersive spectroscopy (EDS). The hardness, wear properties, and corrosion behavior of the fabricated FG samples were also investigated.

2. Materials and Methods

A sample of the research material 180 x 180 x 20 mm was cut from gravity cast AZ91 Mg alloy. The chemical composition of AZ91 Mg alloy was 8.63 Al-0.64 Zn-0.29 Mn-0.08 Si- bal. Mg (in wt. pct.). The sample surface was chemically cleaned prior to processing to remove surface contaminants that could affect the process.

The fabrication of FGNC within the surface of AZ91 Mg alloy was accomplished by vertical milling machine (type Knuth tool milling- Germany), FSP tool, and reinforcement particles (Fig.1). The FSP tool was made from HSS tool steel with a shoulder diameter of 18 mm and a four-sided fluted probe with a height of 6 mm and 4 mm external probe diameter, where the height of the probe can be adjusted. Tilt angle of the FSP tool was set to be 1° in all FSP experiments where the processing tool was rotated clockwise. From our experience in FSP, several tool rotational speeds (830, 960 and 1160 rpm) and a single traverse speed (40 mm/min) with a plunge depth of 0.1 mm were used to make FGNC within the surface of AZ91 Mg alloy.

Tungsten carbide (WC) powder with a median size of 403.4 nm was used as reinforcement particle, as shown in Fig. 2. The WC powder was incorporated into the surface of AZ91 Mg alloy by an innovative multi-stage reduction of chamber diameter (MSRCD) method. The process consisted of creating multi-stage open chambers located in the places where the FSP was carried out. Approximately 60 chambers were drilled for each pass. Each chamber with 3 mm depth had graduated diameters of 3, 2, and 1 mm defined from top to bottom of the chamber as each diameter had a height of 1 mm within the workpiece surface to accommodate the reinforcement particles. The space between successive chambers on the surface of AZ91 Mg alloy was 2 mm. The use of the chambers method was used to prevent, or at least reduce, undesirable displacement of the reinforcement material outside

the processing area, which resulted in dynamic effects between the FSP tool and the reinforcement material. Moreover, this innovative method made it possible to create a gradient distribution of the reinforcing material in the surface of the alloy depending on the processing factors. It should also be noted that the innovative method can be achieved with a single-stage processing using only one processing tool which shortens the processing time.

To study the microstructure and hardness, FG samples were cut in a transverse direction. The surface of the samples was prepared using metallographic techniques including grinding, polishing and then etching with acetic glycol solution. OM as well as SEM equipped with EDS were used to assess the microstructure of the FGNC area and the distribution of WC nanoparticles in the processed zone. The AZ91 Mg alloy phases were analyzed by Shimadzu type X-ray diffractometer (XRD). The XRD spectra were acquired in continuous scanning mode by CuKα irradiation at a scan speed of 5.0 deg/min. The hardness of the FG samples was measured along three parallel lines defined from the outer surface of the processed area and placed near the top surface (~ 0.5 mm), in the center (~ 1.5 mm), and near the bottom of stir zone (~ 2.5 mm) using a digital Vickers micro-hardness machine type TH714. In all the hardness tests, 400 g load was applied for 10 s in which the readings of the hardness values were recorded at successive points for each site with a distance of 0.5 mm from each other.

The wear test was performed utilizing a pin-on-disc test machine by a weight loss method. The specimen to be tested was cut from the FG area with a diameter of 10 mm and a height of 20 mm. The disc was made of hardened steel with a hardness of 60

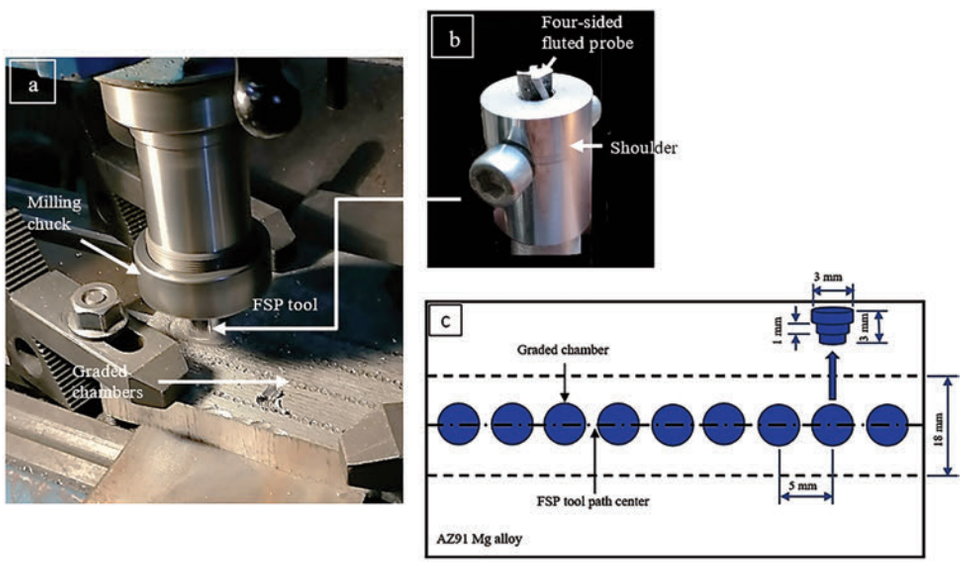

Figure 1. *(a) The fabrication process of FG AZ91/WC nanocomposite using FSP, (b) FSP tool with four-sided fluted probe, (c) Schematic diagram of graded chambers distribution*

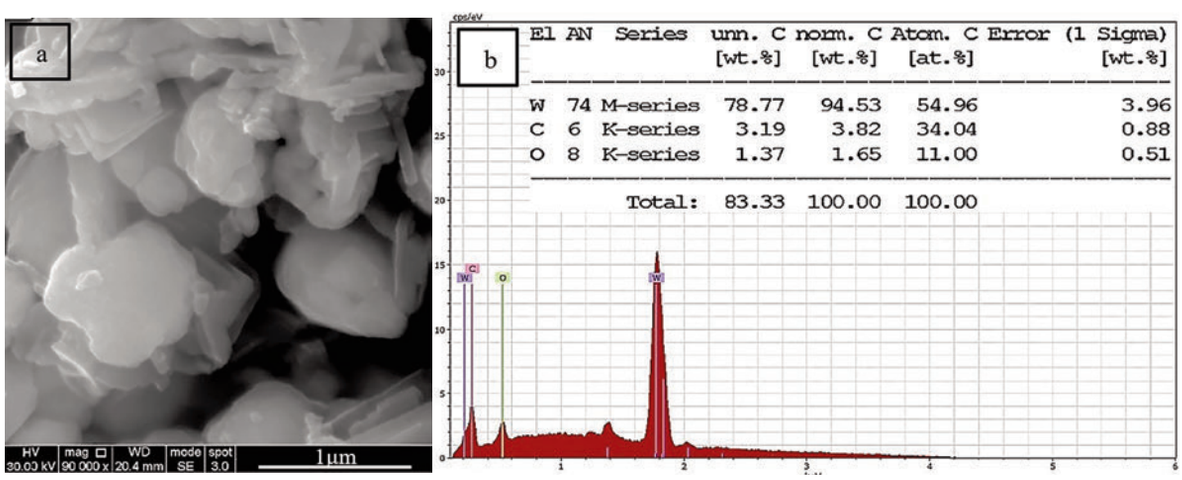

Figure 2. *SEM image (a) and EDS spectrum (b) of WC powder*

HRC whose surface was cleaned before each test with acetone to remove any adherent contaminants. All wear tests were achieved at ambient temperature without lubrication at an applied load of 5 N and a sliding distance of 432597.3 cm. Each wear test was performed for 15 min. The wear mechanism was determined by studying microscopically the topographical features of the worn surface of the tested samples using SEM.

The corrosion properties of the AZ91 Mg and FG samples were investigated using potentiodynamic polarization (PDP) in a 3.5 % NaCl solution at room temperature. Corrosion tests were carried out after the surfaces of the test samples were ground and polished. Three electrodes were used for the PDP experiments, the counter electrode (platinum), the reference electrode (saturated calomel) and the working electrode (samples where a 1 cm^2 area was exposed to the electrolyte). Polarization tests were performed at a scan rate of 2 mV/sec after 1800 s of initial immersion (OCP) and the extrapolation curves were used to analyze the electrochemical parameters. NaCl solution was chosen in corrosion test as it is the most commonly used solution for measuring corrosion behavior in Mg alloys. After contemplating the corrosion test, a SEM was used to examine the corroded surfaces to determine the corrosion mechanism.

3. Results and Discussion

3.1. WC Particles Distribution

A typical display of elemental mapping of FG bead at different rotational speeds is shown in Fig. 3. The EDS mapping of the FG beads clearly described the gradation structure of the different compositions in Fig. 3a, c, e. Generally, good bonding could be recognized between WC nanoparticles and the matrix of the AZ91 Mg alloy, and no cracks were observed in the FG beads. Obviously, WC nanoparticles were distributed throughout the FG bead. It was found that the distribution of WC nanoparticles was done in a gradient manner and higher WC gradient was observed in the upper region of the FG bead. It was evident that the FG bead consisted of three WC gradient regions. The region rich in WC was represented by region 1. In region 2, a continuous WC gradient was found and it was moderate in amount. The region 3 had a lower gradient for WC particles. In all regions, the AZ91 Mg alloy served as a matrix phase. The formation of gradient zones from regions 1 to 3 was due to the multi-stage reduction of the chamber diameter. It was evident that increasing the tool rotation speed from 830 to 1160 rpm increased the gradient distribution and significantly prevented the agglomeration of WC particles within the surface of the AZ91 Mg alloy. Moreover, the increase in the tool rotation speed greater than 830 rpm prevented the formation of the tunneling cavity (TC). The TC was recognized at the bottom of the stir zone at a tool rotation speed of 830 rpm (Fig.3a). The TC was related to the asymmetric material flow in the retreating and advancing sides during the rotation of the tool as the material on the advancing side tended to flow in front of the tool, while material on the retreating side tended to flow back [28]. Therefore, insufficient or asymmetric material flow in the vertical direction, or a delay in filling the cavity could lead to the formation of the TC, which was located in the direction of the processing path. Variations in the composition ratio could be observed in the EDS spectra acquired from FG samples (Fig. 3b, d, f). In addition, these spectra indicated that the intensity of the X-ray emission detected for WC increased gradually from right to left of the structure as different colors of the WC (W and C) increased gradually. The EDS spectra in Fig. 3b, d, f also pointed out to the qualitative presence of each element for the AZ91 Mg alloy such as Mg, Zn, Al, and Mn.

3.2. Microstructure

The microstructure and XRD results of the AZ91 Mg alloy are shown in Fig. 4. It was evident from Fig. 4a that the AZ91 Mg alloy was consisted of two phases based on the XRD result (Fig. 3b). These two phases were α-Mg which represents the matrix (bright portions) and β-$Al_{12}Mg_{17}$ (dark portions). It was noticed that β-$Al_{12}Mg_{17}$ appeared in two forms, mostly as networks distributed at the grain boundaries and a few as particles distributed within the α-Mg matrix. Based on the mean lineal intercept method, the average grain size of the α-Mg alloy was nearly 68 μm.

Figure 5a showed the optical microstructure of different regions of the FG bead. The microstructure of the stir zone (SZ) showed WC particles well bonded to the Mg alloy matrix without the presence of defects. The thermomechanical affected zone (TMAZ) created between the base metal and SZ is shown in Fig. 5b. It was obvious that there was a similar structure between the deformed structure in TMAZ to what was found after cold working. The amount of heat and mechanical strains during processing determined the width of TMAZ whereby an increase in the mechanical strains via increasing tool rotation speed led to an increment in the width of TMAZ [29]. The size of α-Mg decreased as the tool rotational speed decreased from approximately 14 μm at 1160 rpm, 11 μm at 960 rpm to 9 μm at 830 rpm. This could be explained on the basis that the slower the tool rotational speed, the lower the heat generation, and thus the lower the grain growth after dynamic recrystallization. The other reason for α-Mg

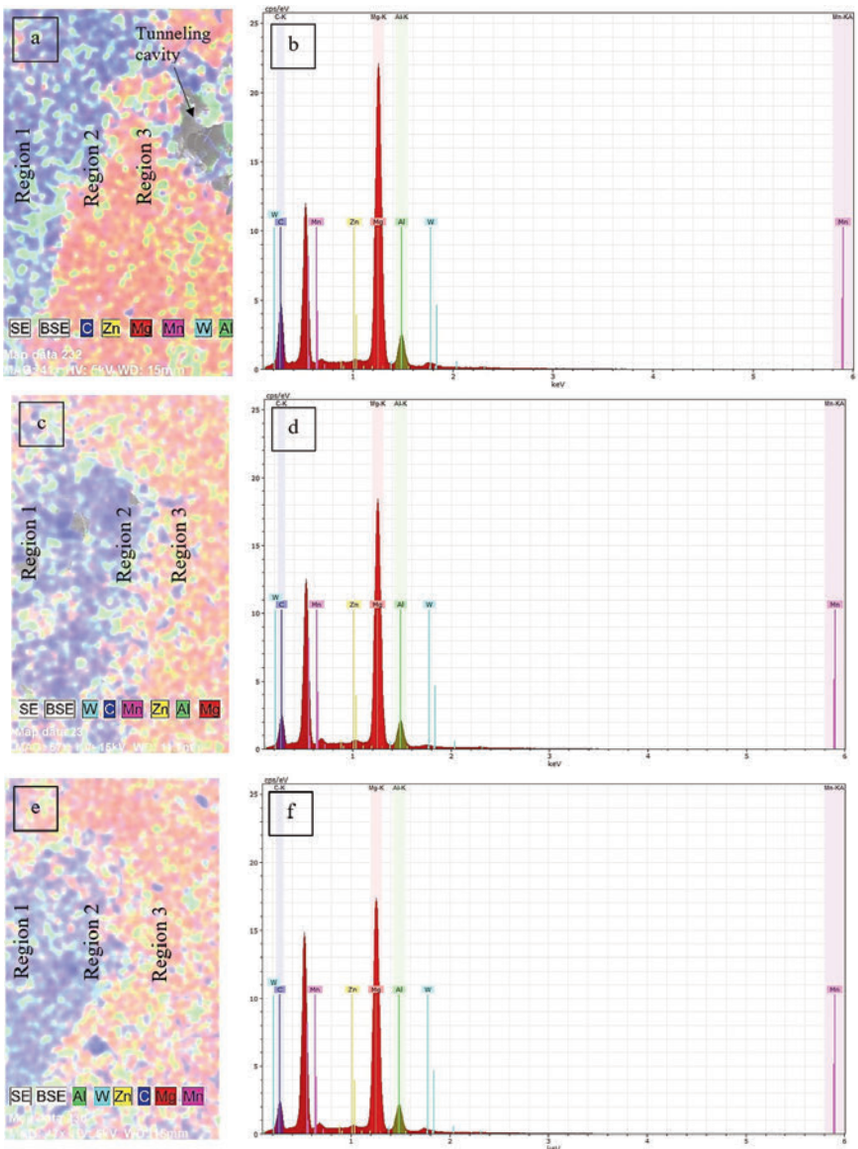

Figure 3. *EDS mapping images and elemental peaks of the FG samples at different tool rotational speeds of (a, b) 830 rpm, (c, d) 960 rpm and (e, f) 1160 rpm*

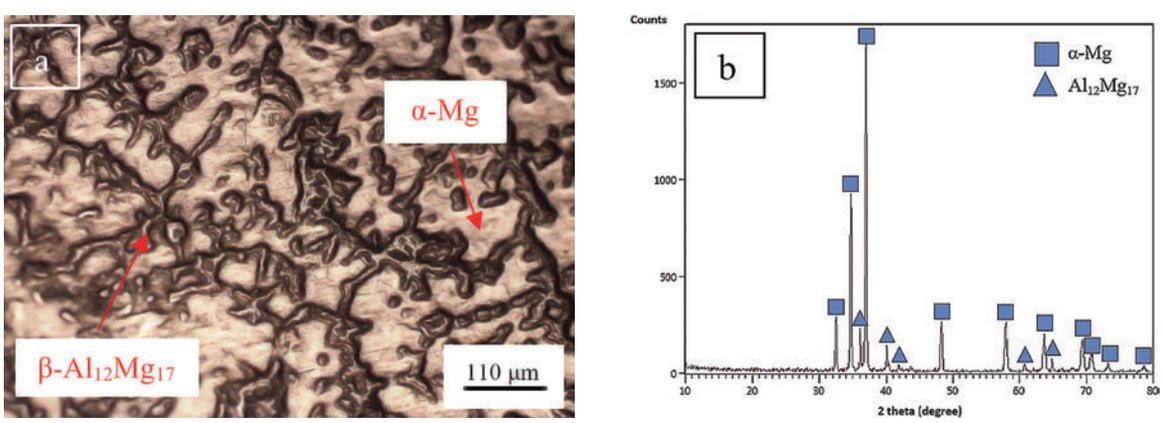

Figure 4. *Microstructure (a) and XRD (b) of AZ91 Mg alloy*

grain reduction with decreasing tool rotational speed was related to the impediment of the dynamic recrystallized grain growth via pinning effect of the WC nanoparticles. Therefore, two mechanisms were involved in achieving α-Mg grain reduction during FGNC fabrication through FSP.

3.3. Hardness Profile

Figure 6 showed the hardness values against the distance measured on the transverse cross-sections of the FG samples where the hardness was increased by adding WC nanoparticles for all the tool rotational speeds used. Moreover, the hardness value decreased with increasing depth from the upper region to the lower region across the intermediate region. In the upper region of the FG bead, the hardness exhibited almost the highest value approximately 126.1, 127.3, and 133.5 HV for tool rotational speeds of 830, 960, and 1160 rpm, respectively. This was found to be nearly 63-73% times higher than that of the average value of the AZ91 Mg alloy basic matrix (77 HV). In the intermediate region, the hardness values of FG samples were 117.5, 117.7, and 128.4 HV for tool rotational speeds of 830, 960, and 1160 rpm,

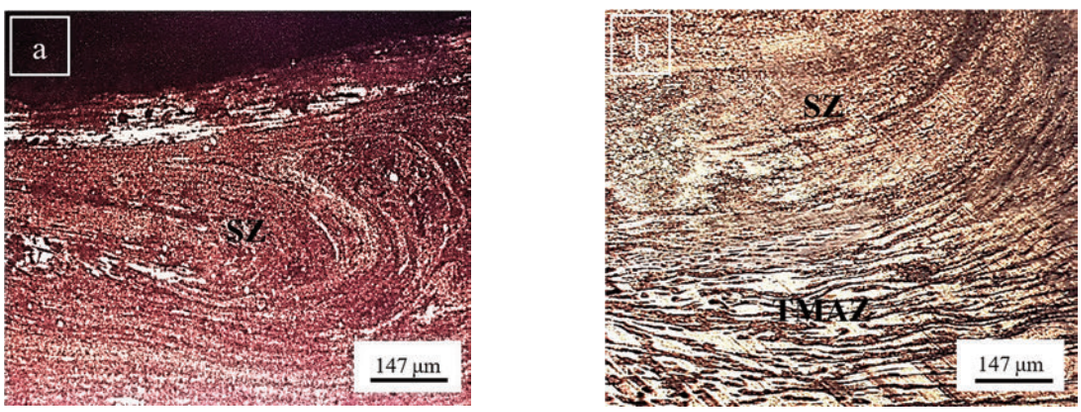

Figure 5. *Optical micrograph of FG bead at tool rotational speed of (a) 1160 rpm and (b) 960 rpm*

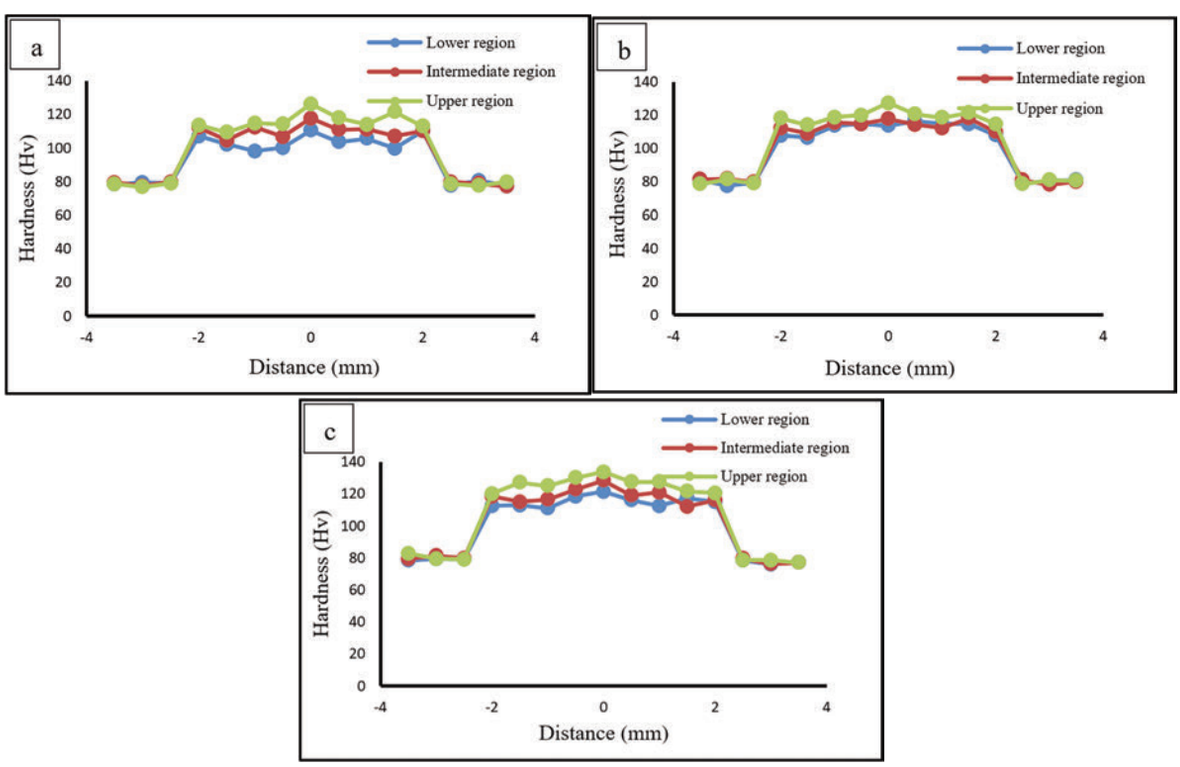

Figure 6. *The correlation between hardness and distance for fabricated FG samples at different tool rotational speeds of (a) 830 rpm, (b) 960 rpm and (c) 1160 rpm*

respectively, which were lower than those in the upper region. In the lower region, the hardness values were significantly decreased to 110.5, 113.6, and 121.4 HV for tool rotational speeds of 830, 960, and 1160 rpm, respectively. Therefore, the gradient distribution of WC nanoparticles in the FG bead played a significant role in the hardness results. This is because the reduction of hardness from the upper region to the lower region might be related to an increase in inter-particle spacing and a reduction in the distribution of WC nanoparticles in the lower region as compared to lower inter-particle spacing and higher distribution of WC nanoparticles in the upper region. Figure 6 also showed that the hardness values were slightly affected by increasing the tool rotational speed from 830 to 1160 rpm for all regions within the FG bead. This means that the added WC particles had the significant role in enhancing the hardness regardless of the amount of heat generated by the rotating tool. Therefore, the improvement in the hardness values could be related to the combination of refinement of the α-Mg grain size caused by the dynamic recrystallization via FSP along with the pinning effect of WC nanoparticles. The variation in the thermal expansion coefficients between different materials, such as AZ91 Mg alloy (26×10^{-6} K^{-1}) [30] and WC particles (~5.5×10^{-6} K^{-1}) [31], results in an increment in the dislocation density [32]. S. Graça et al. [33] showed that the increase in the dislocation density created a hindrance to deformation resulting in an increase in the hardness. It could generally be stated that the improved hardness is attributable to the refinement of the α-Mg grain size and the presence of WC nanoparticles.

3.4. Wear Behavior

Figure 7 showed the wear curve obtained for AZ91 Mg alloy and FG samples fabricated using different tool rotational speeds. It was evident that the AZ91 Mg alloy had a high wear rate value (13.25×10^{-4} g/mm^3) compared to the FG samples. This could be attributed to the lower hardness of the AZ91 Mg alloy compared to that of the FG bead regardless of the region hardness. The hardness of the material is inversely related to the wear rate, i.e., the wear rate diminishes with an augmentation in the hardness value [34]. At a lower tool rotational speed (830 rpm), the FG sample showed a lower wear rate than the AZ91 Mg alloy sample. During dry sliding, WC nanoparticles were commonly presented on the surface and protected the matrix from contact with the counterface surface. Therefore, the WC nanoparticles diminished the wear rate by decreasing the direct applied load on the surface of wear test specimen. At the tool rotational speed of 960 rpm, the wear rate was observed with an additional decrease of the FG sample compared to the AZ91 Mg alloy and FG sample obtained at tool rotational speed of 830 rpm. This could be attributed to the well-bonded WC nanoparticles to the matrix of Mg alloy as well as a high WC nanoparticles gradient reflecting slightly increased hardness. At the higher tool rotational speed (1160 rpm), the wear rate was observed to be lower than the previous samples due to the increased hardness as a result of the presence of WC nanoparticles and α-Mg grain refining.

Figure 8 revealed the worn surface topographies of the AZ91Mg alloy and the FG samples at applied load of 10 N. It showed signs of ploughing which was a major mechanism of material removal. It was evident that the worn surface of the AZ91 Mg alloy was marked by signs of ploughing associated with deep grooves without surface delamination (Fig. 8a). The features of ploughing indicated the phenomenon of abrasive wear. The rolled particles between the mating surfaces or particles adherent to the surface of the counterface acted as abrasives and might have led to the formation of deep grooves resulting in three body abrasive wear-ploughing. Therefore, these severely deformed the surface and the described features of the worn surface were typical of a severe wear. The incorporation of WC nanoparticles into the AZ91 Mg alloy surface led to a significant reduction in the wear rate compared to AZ91 Mg alloy, which was highly dependent on the WC gradient distribution. This is because the presence of WC nanoparticles strengthened the surface of the Mg alloy and thus restricted the deformation and withstood the applied load. The worn surface of the FG sample fabricated at tool rotation speed of 830 rpm showed ploughing surface with detached layer via delamination mechanism (Fig. 8b). The delamination was created by subsurface cracks extending to the external surface of the wear test specimen [35]. The grooves were not

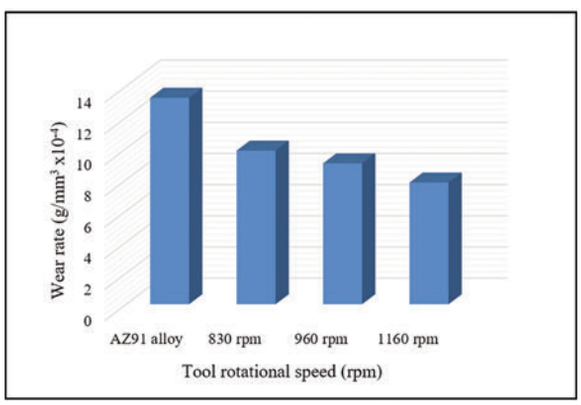

Figure 7. *Wear rate of AZ91Mg alloy and FG samples as a function of tool rotational speed*

as deep as they were identified in AZ91 Mg alloy sample. Wide grooves with shallow depth could be recognized for the FG sample fabricated at 960 rpm (Fig. 8c). These grooves were associated with delamination mechanism. Some particles were adherent to the worn surface and the others could be recognized within the delaminated area. The worn surface of FG sample fabricated at 1160 rpm displayed only shallow grooves with no delaminated areas (Fig. 8d). Also, some particles adherent to the worn surface were identified. All particles adherent to the worn surfaces of FG samples might be WC nanoparticles detached from the worn surface during sliding or related to the Mg alloy separated through wear.

3.5. Corrosion Behavior

Figure 9 showed the potentiodynamic polarization curves of AZ91 Mg alloys and FG samples fabricated with different tool rotational speeds. Generally, each curve included two parts, anodic and cathodic. The anodic part explained the transformation mechanism of the AZ91 Mg alloy surface (passive to breakdown) where Mg dissolved and abnormal anodic hydrogen evolved. In contrast, the cathodic part explained the electrochemical reaction at which hydrogen evolution in the aqueous solution took place where OH^- ions were generated and H_2 gas was released as a result of H_2O molecules accepting electrons. Figure 9 also showed that the corrosion behavior of the samples did not follow a linear relationship, due to the different behavior of the anodic and cathodic areas during corrosion. Moreover, the current density of the anodic area of the AZ91 Mg alloy and FG samples became greater unexpectedly after a certain value. Table 1 showed the electrochemical data obtained from the potentiodynamic polarization curves for AZ91 Mg alloy and FG samples. The sudden increase in current density indicated increasing corrosion and the tendency for galvanic corrosion was inevitable when

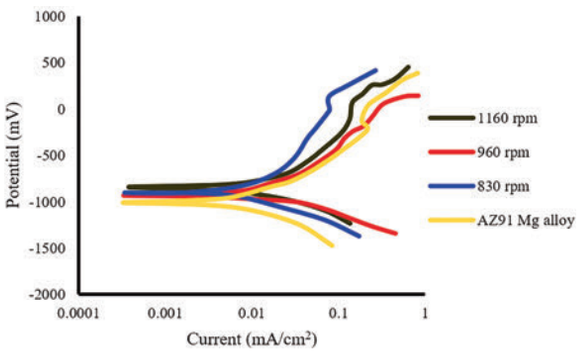

Figure 9. *Potentiodynamic polarization curves of AZ91 Mg alloy and FG samples fabricated at different tool rotational speeds*

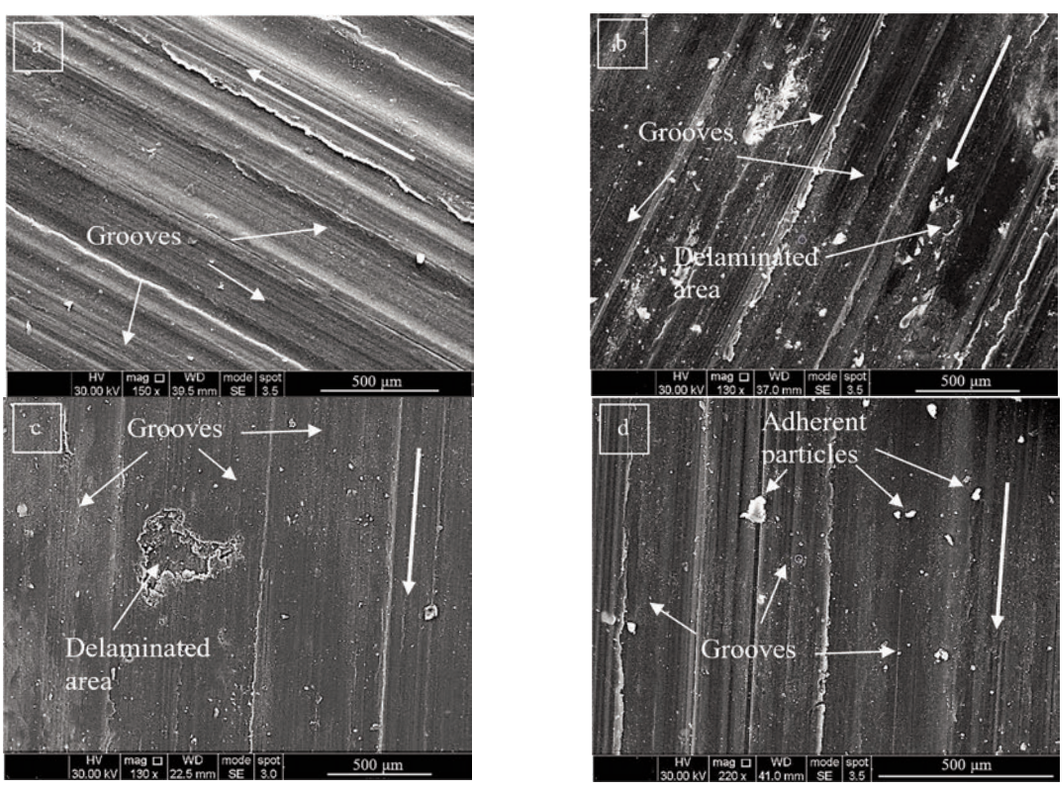

Figure 8. *SEM micrographs of worn surface of (a) AZ91 Mg alloy, and FG samples obtained at tool rotational speeds of (b) 830 rpm, (c) 960 rpm, and (d) 1160 rpm. Arrows indicate sliding direction*

a localized galvanic couple formed between the α-Mg grains and the β-$Al_{12}Mg_{17}$ phase. Frequent breakdown of AZ91 Mg alloy surface, especially in the presence of chloride ions, was a pitting corrosion. The corrosion rate of AZ91 Mg alloy was accelerated when these two processes were combined. The cathodic and anodic curves of the FG samples showed lower current density in the potential range compared to AZ91 Mg alloy. The behavior of the FG samples indicated that the corrosion potential was more positive (noble). Therefore, the FG samples showed enhanced corrosion resistance, along with lower current density and more noble properties, when compared to AZ91 Mg alloy in which any galvanic cell formation would corrode that alloy. The improvement in the corrosion properties of FG samples compared to AZ91 Mg alloy might be due to surface-localized cell removal that could be formed by redistributing α-Mg and the presence of WC particles within the processed area. Another reason could be the release of residual stress from the stirring area during FSP through the annealing effect. It is noteworthy that the rate of current density increase of AZ91 Mg alloy was slower than that of the FG samples.

Table 1. *Electrochemical data obtained from the potentiodynamic polarization curves for samples*

Samples	E_{corr} (mV)	I_{corr} (mA·cm^{-2})
AZ91 Mg alloy	-1030.85	0.010723
FG sample at 830 rpm	-921.96	0.007739
FG sample at 960 rpm	-872.958	0.006941
FG sample at 1160 rpm	-845.735	0.004564

Figure 10 showed the SEM images of an overall view of the corroded surface of AZ91 Mg alloy and FG samples while magnified views revealed minute details. In Fig. 10a, considerable amount of corroded area was observed on AZ91 surface. It was obvious that cracks could be observed within the large pits, shown in the magnified view, as the electrolyte solution came into contact with the matrix material through these cracks and accelerated the rate of corrosion. The corroded surface of the FG sample obtained at the tool rotation speed of 830 rpm (Fig. 8b) had cracks and large pits similar to the corroded surface features of AZ91 Mg alloy implying that both were associated with a similar propensity in the corrosion mechanism (localized galvanic corrosion).

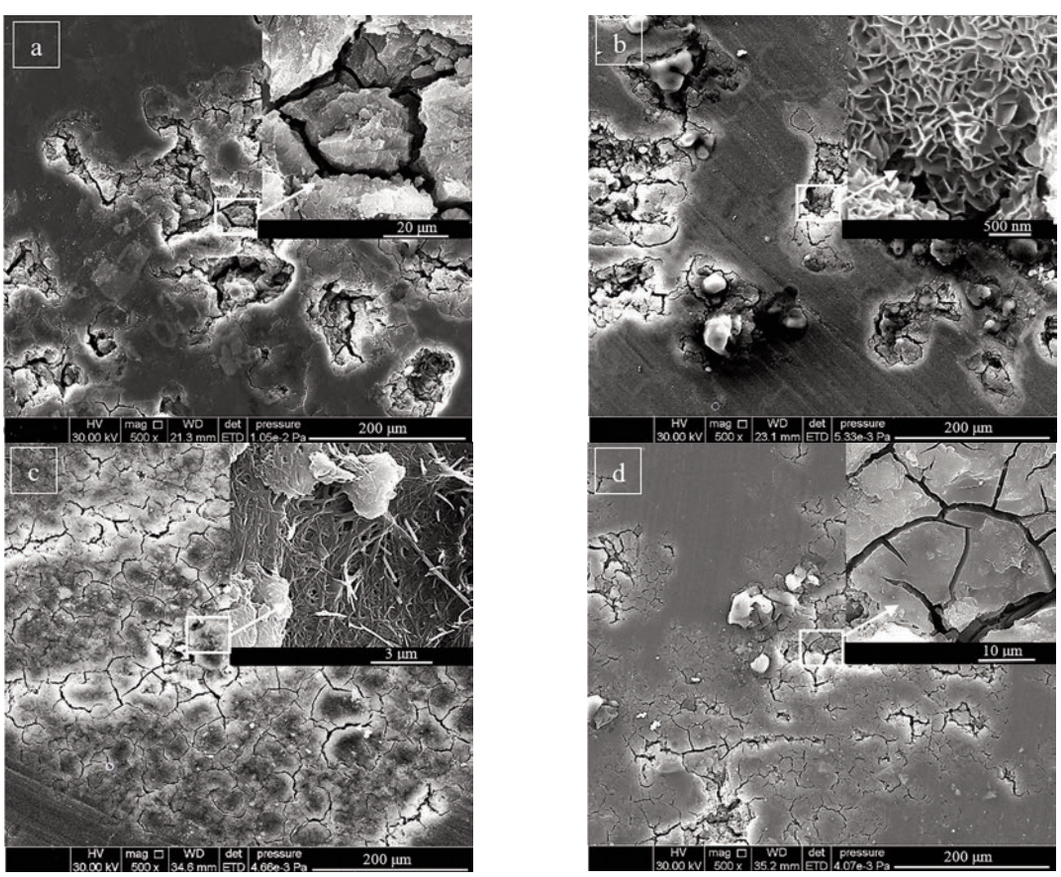

Figure 10. *SEM images of corrosion surfaces of tested samples of (a): AZ91 Mg alloy, and FG samples fabricated at different tool rotational speeds of (b) 830 rpm, (c) 960 rpm, (d) 1160 rpm*

It was also noted that in the magnified view, the corroded surface showed a sponge-like structure within the formed pit. Characterization of the corroded surface of the FG sample made at a tool rotational speed of 960 rpm (Fig. 8c) indicated that it had cracks with clearly low pits formation and a needle-like structure. High magnification view of the needle-like structure showed it as filaments. Increasing the rotation speed of the tool to 1160 rpm made the surface of the FG sample more resistant to corrosion (Fig. 10d), which resulted in reducing the intensity of cracks and pits. The nature of the cracks formed could be observed as in the magnified view of the corroded surface.

4. Conclusions

The present study showed that the MSRCD method in FGNCs fabrication could be performed in a single stage and thus contribute to reducing the fabrication cost and time. The FG samples produced at different tool rotational speeds presented a gradient of the WC distribution. The TC inside the FG bead manufactured at 830 rpm tool rotational speed was identified due to the inadequate speed of the rotating tool. The grain size of α-Mg was directly proportional to the tool rotational speed as the α-Mg grain size was reduced from 14 μm at tool rotational speed of 1160 rpm to 9 μm at the tool rotational speed of 830 rpm. The hardness of FG samples increased significantly towards the outer surface of the FG bead and vice versa. The maximum hardness of FG samples was 133.5 HV close to the outer surface which was obtained at a tool rotational speed of 1160 rpm compared to the hardness of 77 HV for AZ91 Mg alloy. The increment in the hardness of FG samples could be attributed to the refining of the α-Mg grain size and the pinning effect of the WC nanoparticles. Moreover, increasing the speed of the rotating tool slightly affected the hardness value. The FG samples showed improved wear resistance compared to AZ91 Mg alloy due to the presence of WC nanoparticles and the refining effect of α-Mg grain size reflecting the increased hardness. The major wear mechanism of AZ91 Mg alloy and FG samples was the abrasive wear mode. The potentiodynamic polarization curves of the tested samples revealed that the FG sample obtained at the tool rotational speed of 1160 rpm was more corrosion resistant compared to other FG samples and AZ91 Mg alloy. The corroded surface morphology showed that cracks and pits generally appeared on the corrosion surface. Among the various tested samples, the surface of the FG sample obtained at 1160 rpm tool rotational speed had the smallest number of cracks and pits.

Acknowledgments

The authors acknowledge the support and encouragement provided by the University of Technology-Iraq, Dept. of Production Eng. and Metallurgy.

Authorship Contribution Statement

A.D. Subhi: Methodology, Supervision; A.D. Subhi, M.H. Abdulkareem: Data analysis; H.A. Hussein: Experimental work.

Conflict of Interest

The authors declare that they have no conflict of interest.

References

[1] H. Brooks, The relationship between science and technology, Research Policy, 23 (1994) 477-486. https://doi.org/10.1016/0048-7333(94)01001-3

[2] B. Stalin, M. Ravichandran, V. Mohanavel, L.P. Raj, Investigations on microstructure and mechanical properties of Mg-5wt.% Cu-TiB_2 composites produced via powder metallurgy route, Journal of Mining and Metallurgy, Section B: Metallurgy, 56 (2020) 99-108. https://doi.org/10.2298/JMMB190315047S

[3] M.H. Jacobs, Surface engineering of materials, Materials & Design, 14 (1993) 33-37. https://doi.org/10.1016/0261-3069(93)90043-U

[4] M.J. Kadhim, A.D. Subhi, A.A. Moosa, Laser cladding of Inconel 617, 24th International congress on applications of lasers and electro-optics, ICALEO 2005 - Congress Proceedings, (2005) 640-647. https://doi.org/10.2351/1.5060585

[5] V. Boggarapu, R. Gujjala, S. Ojha, S. Acharya, P. Venkateswara babu, S. Chowdary, D. kumar Gara, State of the art in functionally graded materials, Composite Structures, 262 (2021) 113596. https://doi.org/10.1016/j.compstruct.2021.113596

[6] A. Pasha, B.M. Rajaprakash, Functionally graded materials (FGM) fabrication and its potential challenges & applications, Materials Today: Proceedings, 2021. https://doi.org/10.1016/j.matpr.2021.09.077

[7] I.M. El-Galy, B.I. Saleh, M.H. Ahmed, Functionally graded materials classifications and development trends from industrial point of view, SN Applied Sciences, 1 (2019) 1378. https://doi.org/10.1007/s42452-019-1413-4

[8] B.L. Wang, Y.W. Mai, X.H. Zhang, Thermal shock resistance of functionally graded materials, Acta Materialia, 52 (2004) 4961–4972. https://doi.org/10.1016/j.actamat.2004.06.008

[9] J. Abanto-Bueno, J. Lambros, Parameters controlling fracture resistance in functionally graded materials under mode I loading, International Journal of Solids and Structures, 43 (2006) 3920-3939. https://doi.org/10.1016/j.ijsolstr.2005.05.025

[10] A.G. Arsha, E. Jayakumar, T.P.D. Rajan, B.C. Pai,

Processing and characterization of functionally graded in situ aluminum composite, Materials Science Forum, 830-831(2015) 485-488. https://doi.org/10.4028/www.scientific.net/MSF.830-831.485

[11] I. Matuła, G. Dercz, M. Sowa, A. Barylski, P. Duda, Fabrication and characterization of new functional graded material based on Ti, Ta, and Zr by powder metallurgy method, Materials, 14 (2021) 6609. https://doi.org/10.3390/ma14216609

[12] C. Zhou, P. Wang, W. Li, Fabrication of functionally graded porous polymer via supercritical CO_2 foaming, Composites Part B: Engineering, 42 (2011) 318-325. https://doi.org/10.1016/j.compositesb.2010.11.001

[13] K. Maile, K. Berreth, A. Lyutovich, Functionally graded coatings of carbon reinforced carbon by physical and chemical vapour deposition (PVD and CVD), Materials Science Forum, 492-493 (2005) 347-352. https://doi.org/10.4028/www.scientific.net/MSF.492-493.347

[14] H. Xing, B. Zou, X. Liu, X. Wang, C. Huang, Y. Hu, Fabrication strategy of complicated Al_2O_3-Si_3N_4 functionally graded materials by stereolithography 3D printing, Journal of the European Ceramic Society, 40 (2020) 5797-5809. https://doi.org/10.1016/j.jeurceramsoc.2020.05.022

[15] E. Askari, M. Mehrali, I.H.S.C. Metselaar, N.A. Kadri, Md.M. Rahman, Fabrication and mechanical properties of Al_2O_3/SiC/ZrO_2 functionally graded material by electrophoretic deposition, Journal of the Mechanical Behavior of Biomedical Materials, 12 (2012) 144-150. https://doi.org/10.1016/j.jmbbm.2012.02.029

[16] J. Gandra, R. Miranda, P. Vilaça, A. Velhinho, J.P. Teixeira, Functionally graded materials produced by friction stir processing, Journal of Materials Processing Technology, 211 (2011) 1659-166. https://doi.org/10.1016/j.jmatprotec.2011.04.016

[17] R.M. Miranda, T.G. Santos, J. Gandra, N. Lopes, R.J.C. Silva, Reinforcement strategies for producing functionally graded materials by friction stir processing in aluminium alloys, Journal of Materials Processing Technology, 213 (2013) 1609-1615. https://doi.org/10.1016/j.jmatprotec.2013.03.022

[18] M.H. Mohammed, A.D. Subhi, Exploring the influence of process parameters on the properties of SiC/A380 Al alloy surface composite fabricated by friction stir processing, Engineering Science and Technology, an International Journal, 24 (2021) 1272-1280. https://doi.org/10.1016/j.jestch.2021.02.013

[19] B. Saleh, J. Jiang, R. Fathi, T. Al-hababi, Q. Xu, L. Wang, D. Song, A. Ma, 30 Years of functionally graded materials: An overview of manufacturing methods, Applications and Future Challenges, Composites Part B, 201 (2020) 108376. https://doi.org/10.1016/j.compositesb.2020.108376

[20] A. Yang, K.B. Nie, K.K. Deng, J.G. Han, T. Xiao, X.Z. Han, Microstructures and tensile properties of Mg-2Zn-0.8Sr-0.2Ca alloy extruded at relatively slow speed and low temperature, Journal of Mining and Metallurgy, Section B: Metallurgy, 58 (2022) 203-218. https://doi.org/10.2298/JMMB210325004Y

[21] I. Dinaharan, S. Zhang, G. Chen, Q. Shi, Assessment of Ti-6Al-4V particles as a reinforcement for AZ31 magnesium alloy-based composites to boost ductility incorporated through friction stir processing, Journal of Magnesium and Alloys, 10 (2022) 979-992. https://doi.org/10.1016/j.jma.2020.09.026

[22] B.R. Sunil, G.P.K. Reddy, H. Patle, R. Dumpala, Magnesium based surface metal matrix composites by friction stir processing, Journal of Magnesium and Alloys, 4 (2016) 52-61. http://doi.org/10.1016/j.jma.2016.02.001

[23] M. Sam, R. Jojith, N. Radhika, Progression in manufacturing of functionally graded materials and impact of thermal treatment-A critical review, Journal of Manufacturing Processes, 68 (2021) 1339-1377. https://doi.org/10.1016/j.jmapro.2021.06.062

[24] R.K. Singh, V. Rastogi, A review on solid state fabrication methods and property characterization of functionally graded materials, Materials Today: Proceedings, 47 (2021) 3930-3935. http://doi.org/10.1016/j.matpr.2021.03.634

[25] M. Salehi, H. Farnoush, J.A. Mohandesi, Fabrication and characterization of functionally graded Al–SiC nanocomposite by using a novel multistep friction stir processing, Materials and Design, 63 (2014) 419-426. http://doi.org/10.1016/j.matdes.2014.06.013

[26] V. Bikkina, S.R. Talasila, K. Adepu, Characterization of aluminum based functionally graded composites developed via friction stir processing, Transactions of Nonferrous Metals Society of China, 30 (2020) 1743-1755. http://doi.org/10.1016/S1003-6326(20)65335-3

[27] A.M. Jamili, A. Zarei-Hanzaki, H.R. Abedi, P. Minarik, Development of grain size/texture graded microstructures through friction stir processing and subsequent cold compression of a rare earth bearing magnesium alloy, Materials Science & Engineering, A 814 (2021) 141190. https://doi.org/10.1016/j.msea.2021.141190

[28] A.A.F. Hoda, N.B. Mostafa Arab, M.H. Gollo, B. Nami, Numerical and experimental investigation of defects formation during friction stir processing on AZ91, SN Applied Sciences, 3 (2021) 108. https://doi.org/10.1007/s42452-020-04032-y

[29] P. Zolghadr, M. Akbari, P. Asadi, Formation of thermo-mechanically affected zone in friction stir welding, Materials Research Express, 6 (2019) 086558. https://doi.org/10.1088/2053-1591/ab1d25

[30] D.H. Cho, J.H. Nam, B.W. Lee, S.O. Yim, I.M. Park, Thermal expansion properties of carbon nanotube/silicon carbide particle-reinforced magnesium composites fabricated by squeeze infiltration, Metals and Materials International, 22 (2016) 332-339. https://doi.org/10.1007/s12540-016-5454-6

[31] A.S. Kurlov, A.I. Gusev, Tungsten carbides: structure, properties and application in hardmetals, Springer, Switzerland, 2013. pp.1-3.

[32] Z. Trojanová, Z. Drozd, P. Lukáˇc, P. Minárik, G. Németh, S. Seetharaman, J. Džugan, M. Gupta, Magnesium reinforced with Inconel 718 particles prepared ex situ - microstructure and properties, Materials, 13 (2020) 798. https://doi.org/10.3390/ma13030798

[33] S. Graça, R. Colaço, P.A. Carvalho, R. Vilar, Determination of dislocation density from hardness measurements in metals, Materials Letters, 62 (2008) 3812-3814. https://doi.org/10.1016/j.matlet.2008.04.072

[34] A.D. Subhi, A.A. Khleif, Q.S. Abdul-Wahid, Microstructural investigation and wear characteristics

of Al-Si-Ti cast alloys, Engineering Transactions, 68 (2020) 385-395. https://doi.org/10.24423/EngTrans.1156.20201029

[35] B. Kılınç, E. Kocaman, Ş. Şen, U. Şen, Effect of titanium content on the microstructure and wear behavior of Fe(13-x)TixB7 (x=0-5) hardfacing alloy, Journal of Mining and Metallurgy, Section B: Metallurgy, 58 (2022) 29-41. https://doi.org/10.2298/JMMB210430047K

FUNKCIONALNO KLASIFIKOVANI AZ91/VC NANOKOMPOZIT PROIZVEDEN FRIKCIONIM POSTUPKOM SA MEŠANJEM NA INOVATIVAN NAČIN

A.D. Subhi*, M.H. Abdulkareem, H.A. Hussein

Tehnološki univerzitet- Irak, Odsek za proizvodno inženjerstvo i metalurgiju, Bagdad, Irak

Apstrakt

U ovom radu, funkcionalno klasifikovani AZ91/VC nanokompoziti su pripremljeni inovativnom metodom smanjenja prečnika komore u više koraka. WC nanočestice su spakovane u komore sa gradiranim veličinama prečnika i obrađene frikcionim postupkom sa mešanjem uz pomoć četvorostrano žlebljene sonde. Funkcionalno klasifikovani nanokompoziti su proizvedeni pri različitim brzinama rotacije alata (830, 960 i 1160 o/min) pri konstantnoj brzini pomaka i dubini uranjanja od 40 mm/min i 0,1 mm, pojedinačno. Osobine funkcionalno klasifikovanih uzoraka i legure AZ91 Mg ispitivane su optičkom i skenirajućom elektronskom mikroskopijom, energetski disperzivnom spektroskopijom i drugim metodama kao što je merenje tvrdoće, ispitivanje habanja metodom igle i diska, kao i određivanje potenciodinamičke polarizacije. Rezultati su pokazali da se α -Mg i stepenovana distribucija WC nanočestica poboljšavaju kako se brzina rotacije alata povećava. Tvrdoća je blago porasla sa povećanjem brzine rotacije alata. Rezultati su takođe pokazali da je stopa habanja smanjena i otpornost na koroziju poboljšana dodavanjem WC nanočestica. Režim abrazivnog habanja bio je glavni način uklanjanja materijala tokom suvog klizanja, dok su pukotine i udubljenja bile glavne karakteristike korodirane površine.

Ključne reči: *Frikcioni proces sa mešanjem; Funkcionalno klasifikovan kompozit; Nanokompozit; AZ91 Mg legura; Volfram karbid*